Supplementary Material for:

”Manipulable multi-purpose nanothermometers based on a fluorescent hybrid glass fiber microsphere cavity”

Dandan Yang[a], Jianhao Chen[a], Jiachang Wu[a], Hao Zhang[a], Xiaofeng Liu[b], Jianrong Qiu[c], Zhongmin Yang[d], Guoping Dong[a*]

[a]South China University of Technology, School of Materials Science and Engineering, State Key Laboratory of Luminescent Materials and Devices, Wushan Road 381, Guangzhou, China, 510641

[b]Zhejiang University, School of Materials Science and Engineering, Yuhangtang Road 866, Hangzhou, China, 310058

[c]Zhejiang University, College of Optical Science and Engineering, State Key Laboratory of Modern Optical Instrumentation, Zheda Road 38, Hangzhou, China, 310027

[d]South China University of Technology, School of Physics and Optoelectronics, Wushan Road 381, Guangzhou, China, 510641

*Guoping Dong, E-mail: dgp@scut.edu.cn

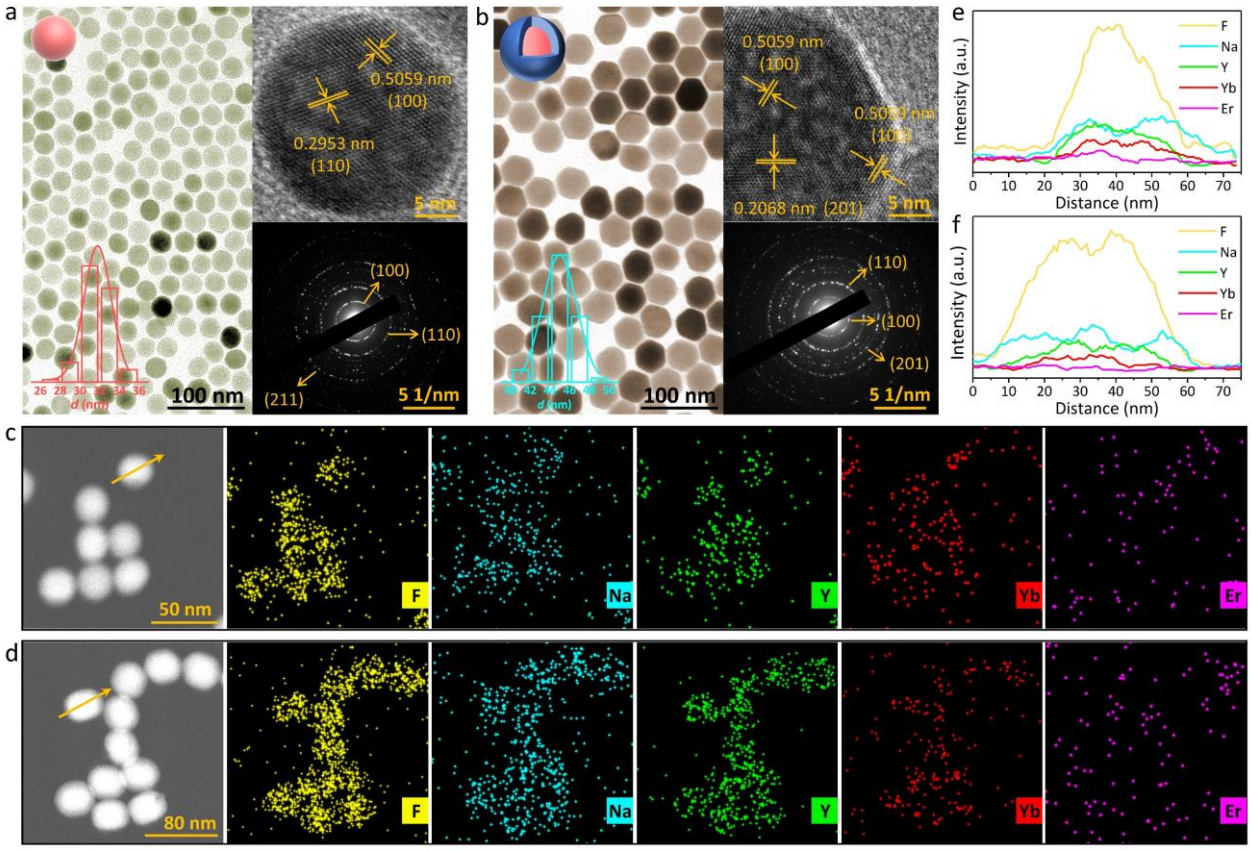

Fig. S1 (a) and (b) Transmission electron microscopy (TEM), high-resolution TEM and selected-area electron diffraction images of the as-synthesized (a) $NaYF_4$:20%Yb^{3+},2%Er^{3+} core and (b) $NaYF_4$:20%Yb^{3+},2%Er^{3+}@$NaYF_4$ core-shell NCs. The insets at the top left are the schematic of the core and core-shell structure. The insets at the bottom left show the size distribution of corresponding NCs together with a Gaussian fitting. (c) and (d) High-angle annular dark-field scanning transmission electron microscopy and corresponding element distribution of the as-synthesized (c) $NaYF_4$:20%Yb^{3+},2%Er^{3+} core and (d) $NaYF_4$:20%Yb^{3+},2%Er^{3+}@$NaYF_4$ core-shell NCs. (e) and (f) Line scanning spectra along the yellow scan line in (c) and (d) for different elements of the as-synthesized (e) $NaYF_4$:20%Yb^{3+},2%Er^{3+} core and (f) $NaYF_4$:20%Yb^{3+},2%Er^{3+}@$NaYF_4$ core-shell NCs.

This Figure confirms the morphology and microstructure of the as-synthesized Er^{3+}-Yb^{3+} co-doped $NaYF_4$ nanocrystals (NCs). The as-synthesized $NaYF_4$:20%Yb^{3+},2%Er^{3+} core and $NaYF_4$:20%Yb^{3+},2%Er^{3+}@$NaYF_4$ core-shell NCs with a hexagonal structure exhibit a monodisperse spherical morphology with average sizes of 32 nm and 45 nm, respectively. The observation of well-defined lattice fringes reveals their good crystalline properties. Besides an increment in size, the core-shell structure is also evidenced by the distribution of each lanthanide element.

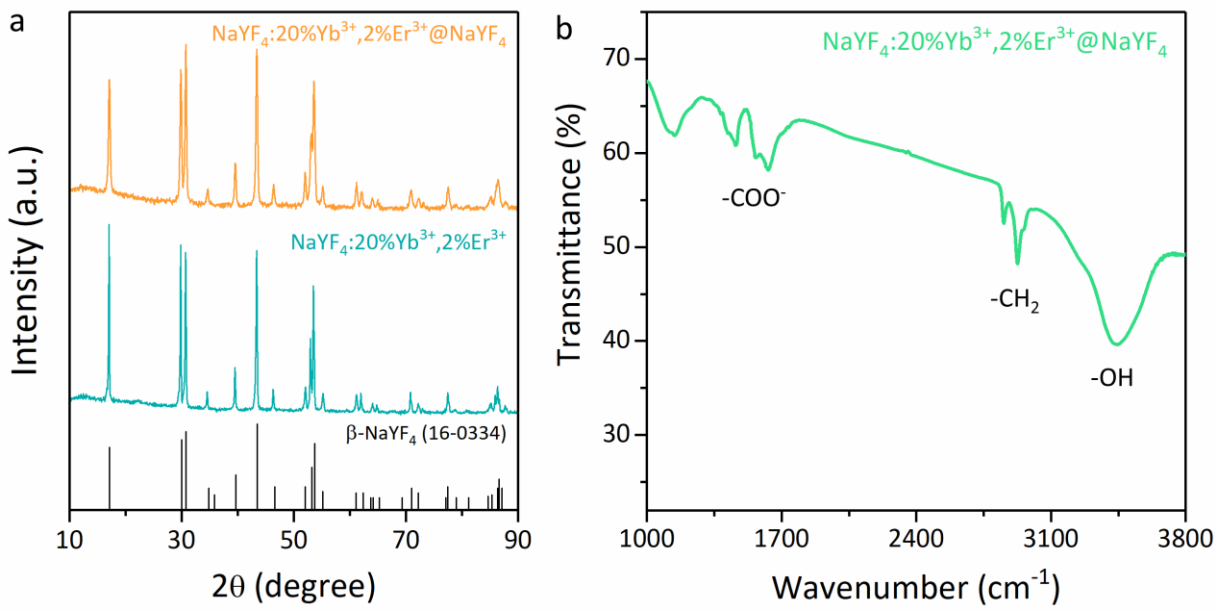

Fig. S2 (a) X-ray diffraction (XRD) patterns of the as-synthesized $NaYF_4$:20%Yb^{3+},2%Er^{3+} core and $NaYF_4$:20%Yb^{3+},2%Er^{3+}@$NaYF_4$ core-shell NCs. (b) Fourier-transform infrared spectrum of the as-synthesized $NaYF_4$:20%Yb^{3+},2%Er^{3+}@$NaYF_4$ core-shell NCs.

Due to the use of oleic acid (OA) and 1-octadecene (ODE) during the synthetic process, different organic ligands are anchored to the surface of the as-synthesized $NaYF_4$:20%Yb^{3+},2%Er^{3+}@$NaYF_4$ NCs, which is confirmed by the presence of the asymmetric (ν_{as}) and symmetric (ν_s) -COO^- group at ~1630 cm^{-1} and ~1459 cm^{-1}, the asymmetric (ν_{as}) and symmetric (ν_s) methylene (-CH_2) group at ~2926 cm^{-1} and ~2854 cm^{-1}, and the stretching vibrating hydroxyl group (-OH) at ~3448 cm^{-1}.[45]

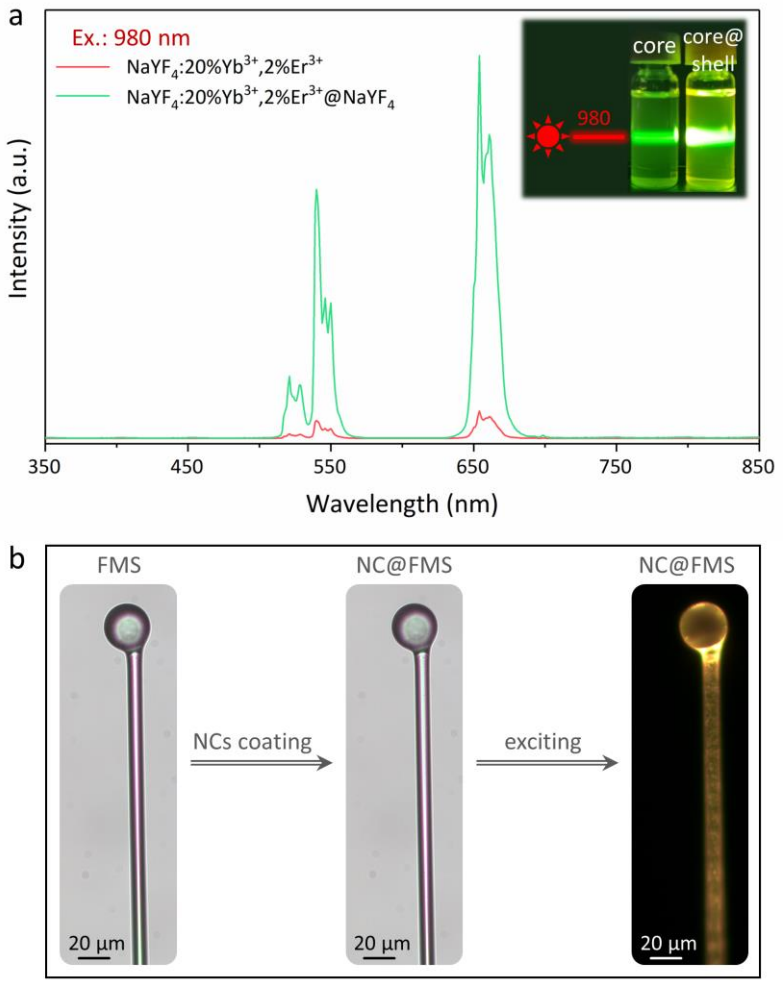

Fig. S3 (a) Upconversion photoluminescence (PL) spectra of the as-synthesized $NaYF_4$:20%Yb^{3+},2%Er^{3+} core and $NaYF_4$:20%Yb^{3+},2%Er^{3+}@$NaYF_4$ core-shell NCs upon 980 nm excitation. The inset is the corresponding fluorescent photograph. (b) Microscopic photographs of a silica fiber microsphere (FMS) and a $NaYF_4$:20%Yb^{3+},2%Er^{3+}@$NaYF_4$ NCs coated FMS (NC@FMS), as well as the microscopic fluorescent photograph of the NC@FMS excited by the designed all-fiber optical path with a 980 nm fiber laser as excitation source.

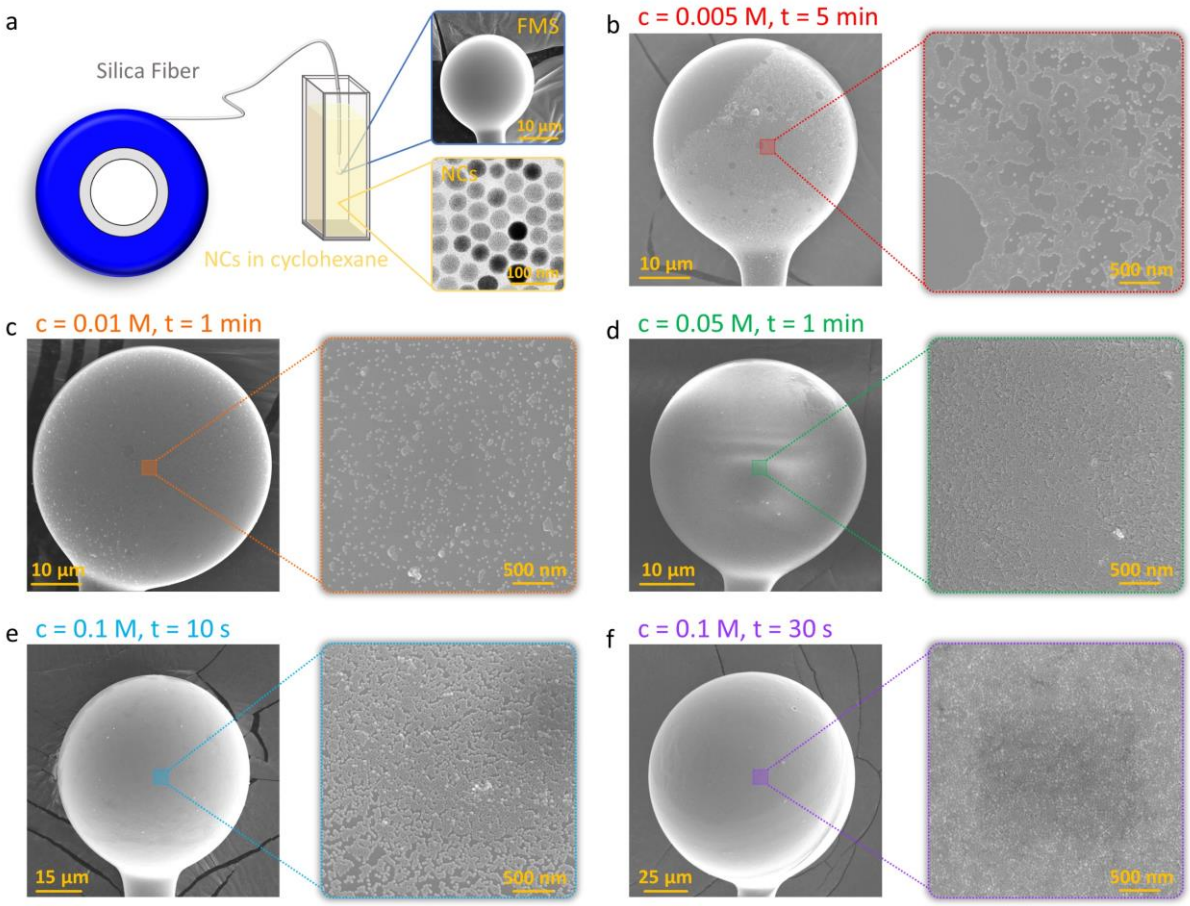

Fig. S4 (a) Schematic illustrating the fabrication method of the NC@FMS. The insets show the scanning electron microscopy (SEM) image of an FMS and TEM image of the as-synthesized NCs. (b-f) SEM images of NC@FMSs and their surface structures obtained at different NC dispersion concentrations in cyclohexane and immersing times.

The increased surface roughness of the FMS resulting from the coated NCs will induce scattering losses and reduce quality factors. Homogeneous coating can avoid aggregations and minimize scattering,[19] which is related to the NC concentration and immersing time. Therefore, we immersed FMSs with different diameters into the cyclohexane dispersions of different NC concentrations for different time. As shown in this Figure, a high NC concentration is beneficial to acquire homogeneous coating. For example, in a cyclohexane dispersion with a NC concentration of 0.1 M, only 30 s is needed for homogeneous coating of an FMS with a diameter of ~100 μm. Consequently, in the following demonstration, we prepared NC@FMSs using the NC concentration of 0.1 M and selected the immersing time according to the FMS diameter.

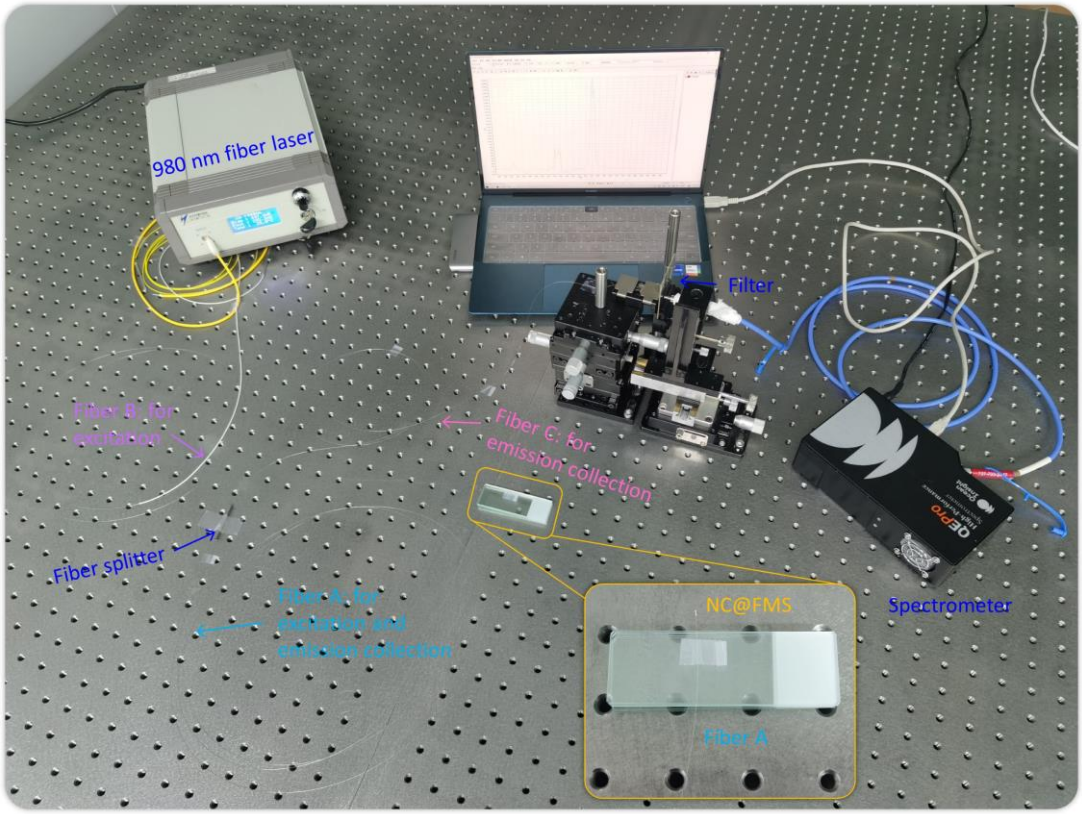

Fig. S5 Photograph of the lab-made NC@FMS all-fiber sensor measurement system.

Although excitation and emission lights can concurrently transmit in tail fiber of FMS, the tail fiber cannot connect with the excitation and detection device at the same time. To circumvent this problem and achieve all-fiber operation, we introduced a fiber splitter fabricated with the same commercial silica fiber, which splits the one fiber optical path into two identical fiber optical paths. As demonstrated in this Figure and Fig. 1, the single fiber end of the fiber splitter is fused with the tail fiber of the FMS (labeled as Fiber A) for the simultaneous transmission of excitation and emission lights. While for the splitter ends, one (labeled as Fiber B) is fused with a fiber excitation source and mainly transmits excitation light, the other (labeled as Fiber C) is docked to a fiber spectrometer and mainly used for the analysis of emission signals. Thus, the excitation light is coupled into the FMS through the transmission of Fiber A and B and randomly reflects on the inner surface of the FMS. Due to a comparable refractive index between the silica glass and $NaYF_4$ host,[31] the excitation light is leaked to the outer surface to excite the surface NCs, and the emission lights from the surface NCs

are coupled into the FMS and further coupled into the Fiber A also by the random reflection. After transmission by Fiber A and C, the emission lights are captured by a spectrometer for following signal reading. A high-pass filter is added between the Fiber C and fiber spectrometer to avoid an interference from excitation light to detection signals.

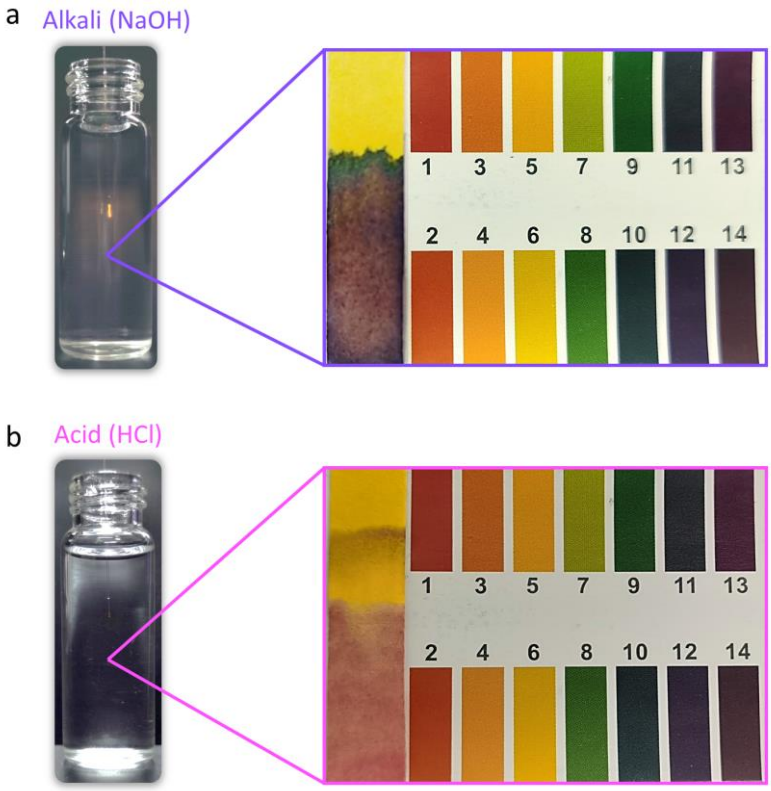

Fig. S6 PH testing of the (a) alkaline and (b) acidic environments where the NC@FMS all-fiber sensor is employed.

In this work, the acidic solution was prepared by diluting concentrated hydrochloric acid (HCl) with water, and the alkaline solution was prepared by dissolving the appropriate amount of NaOH salt into water.

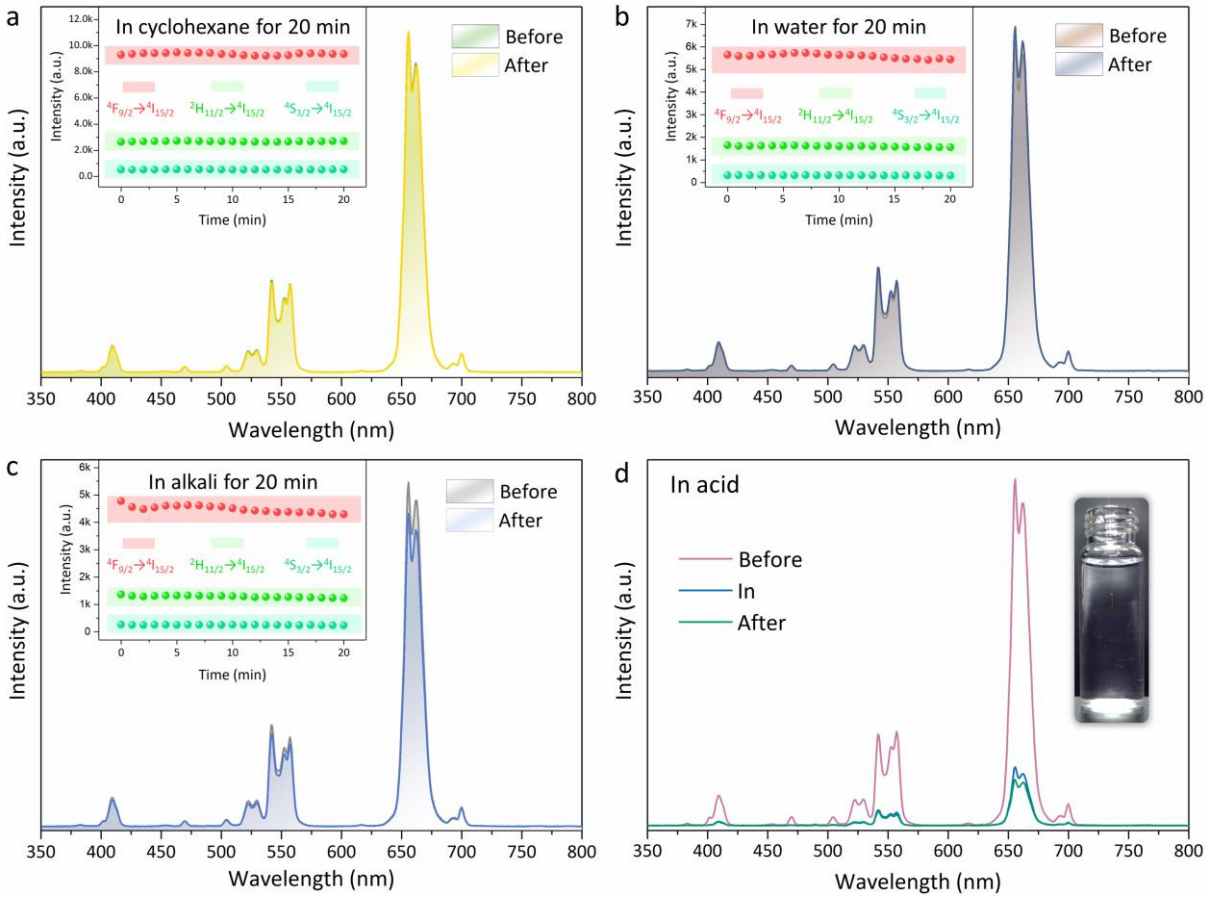

Fig. S7 (a-c) PL spectra of $NaYF_4$:20%Yb^{3+},2%Er^{3+}@$NaYF_4$ NC@FMS all-fiber sensors before and after immersing in different environments for 20 min: (a) in cyclohexane; (b) in water; (c) in alkali. The insets are emission intensity fluctuations of these NC@FMS all-fiber sensors over time when in the corresponding environment. (d) PL spectra of a $NaYF_4$:20%Yb^{3+},2%Er^{3+}@$NaYF_4$ NC@FMS all-fiber sensor before, during, and after immersing in an acidic environment. The inset displays the fluorescent photograph of the NC@FMS in the acidic environment.

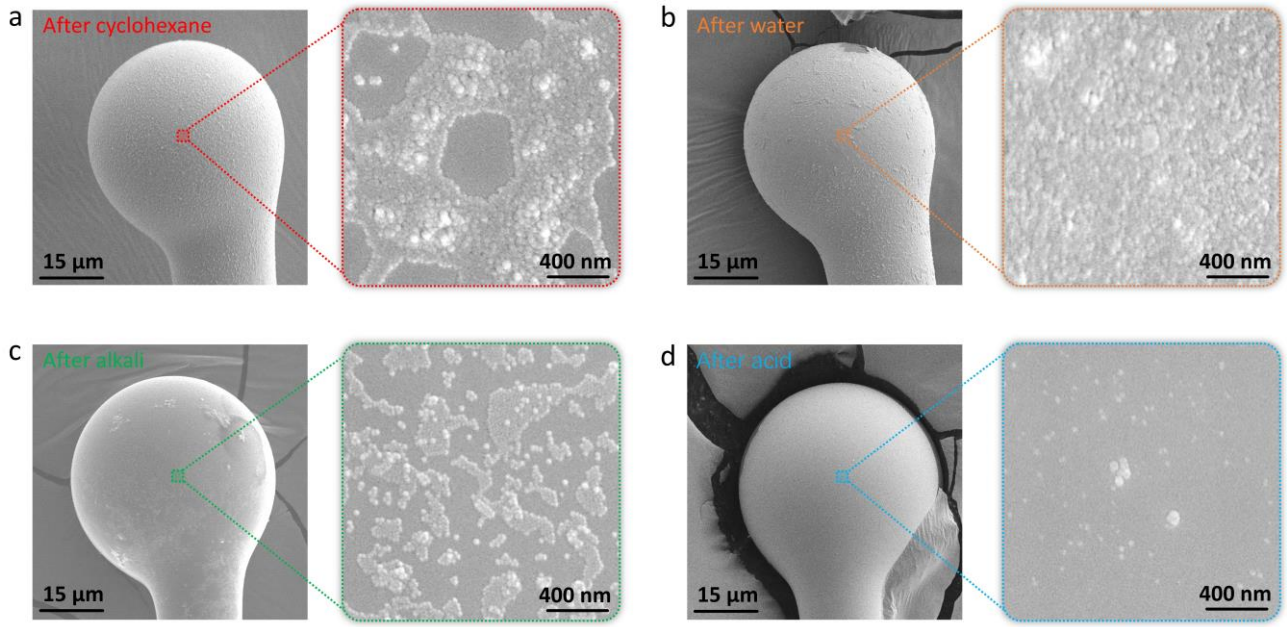

Fig. S8 (a-c) SEM images of $NaYF_4$:20%Yb^{3+},2%Er^{3+}@$NaYF_4$NC@FMSs and their surface structures after immersing in (a) cyclohexane, (b) water, and (c) alkali for 20 min, respectively. (d) SEM images of a $NaYF_4$:20%Yb^{3+},2%Er^{3+}@$NaYF_4$ NC@FMS and its surface structures after immersing in acid for 10 s.

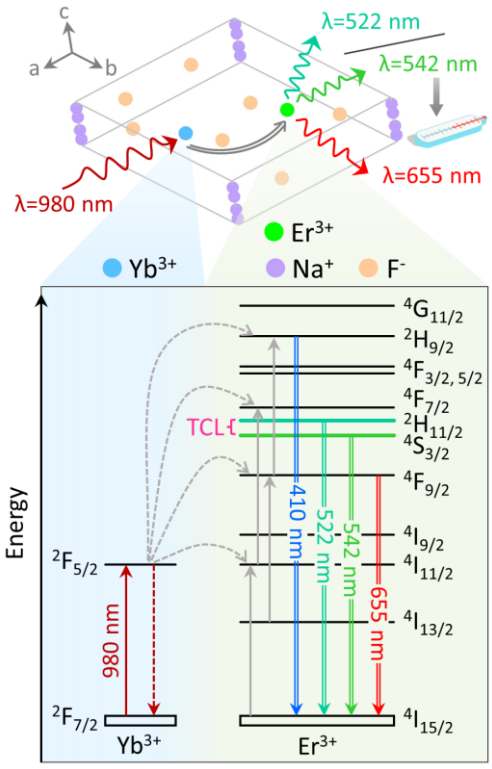

Fig. S9 Crystallographic structure, energy level diagram, and proposed energy transfer mechanisms between Yb^{3+} and Er^{3+} in the as-synthesized NCs under 980 nm excitation.

As shown in this Figure, when the as-synthesized NCs are excited by 980 nm, the Yb^{3+} strongly absorbs the incident 980 nm photons and emits broad-band resonant photons that help the electrons in the Er^{3+}:$^4I_{15/2}$ level to be excited to the excited states. Successive transfers of three photons induce a population of $^2H_{9/2}$ level, and two successive energy transfers induce a population in the $^2H_{11/2}$, $^4S_{3/2}$, and $^4F_{9/2}$ levels. The electrons in these levels relaxing to the ground state realize blue, green, and red upconverted emissions.

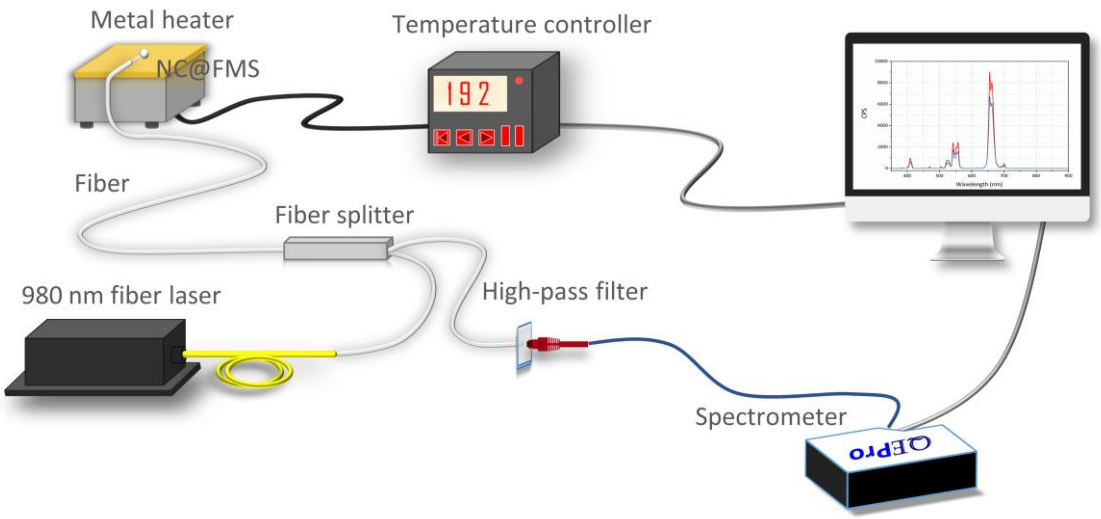

Fig. S10 Schematic diagram of the thermometric performance measurement of the designed NC@FMS all-fiber sensors.

Table S1 Relative sensitivity (S_r) and detection ranges in reported Er^{3+}-doped upconversion nanothermometers based on the $^4S_{3/2}/^2H_{11/2}$ thermally coupled levels.

Host	T [K]	S_r [$\%K^{-1}$]	Ref.
β-$NaYF_4$@$NaYF_4$	225-465	$1027/T^2$	This work
Annealed β-$NaYF_4$@$NaYF_4$	195-510	$1051/T^2$	This work
YF_3	260-490	$949.7/T^2$	[46]
β-$NaYF_4$	300-600	$777.9/T^2$	[47]
α-$NaYF_4$	303-743	$1042.7/T^2$	[48]
YOF	260-490	$984.9/T^2$	[49]
Y_2O_3	260-490	$1073.4/T^2$	[49]
$CaSc_2O_4$	299-623	$1083.9/T^2$	[50]
$GdVO_4$	307-473	$997.5/T^2$	[51]
$NaY(WO_4)_2$	293-503	$1073.1/T^2$	[52]
$Y_2Mo_4O_{15}$	289-483	$992.2/T^2$	[53]

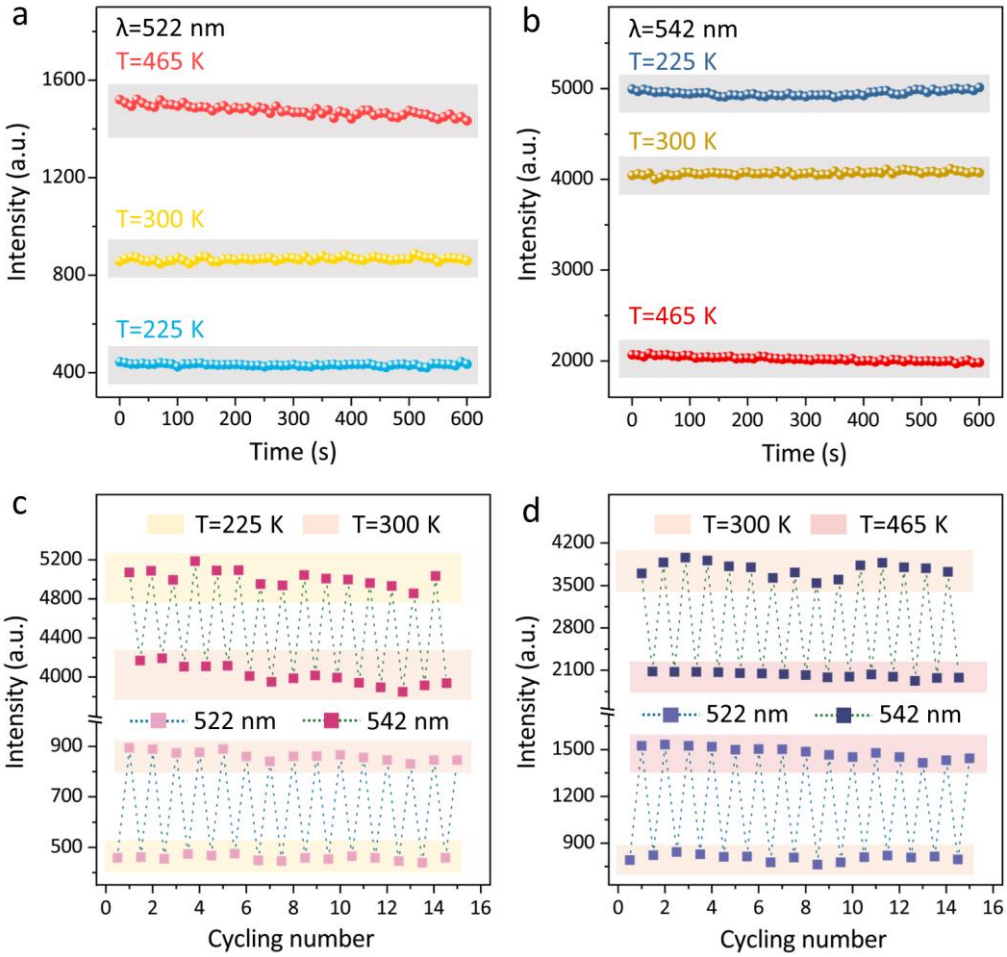

Fig. S11 (a) and (b) Emission intensity fluctuations at (a) 522 nm and (b) 542 nm of the $NaYF_4$:20%Yb^{3+},2%Er^{3+}@$NaYF_4$ NC@FMS all-fiber sensor over time at the constant temperatures of 225, 300, and 465 K. (c) and (d) Emission intensity cycling test at 522 nm and 542 nm of the $NaYF_4$:20%Yb^{3+},2%Er^{3+}@$NaYF_4$ NC@FMS all-fiber sensor between (c) 225-300 K and (d) 300-465 K.

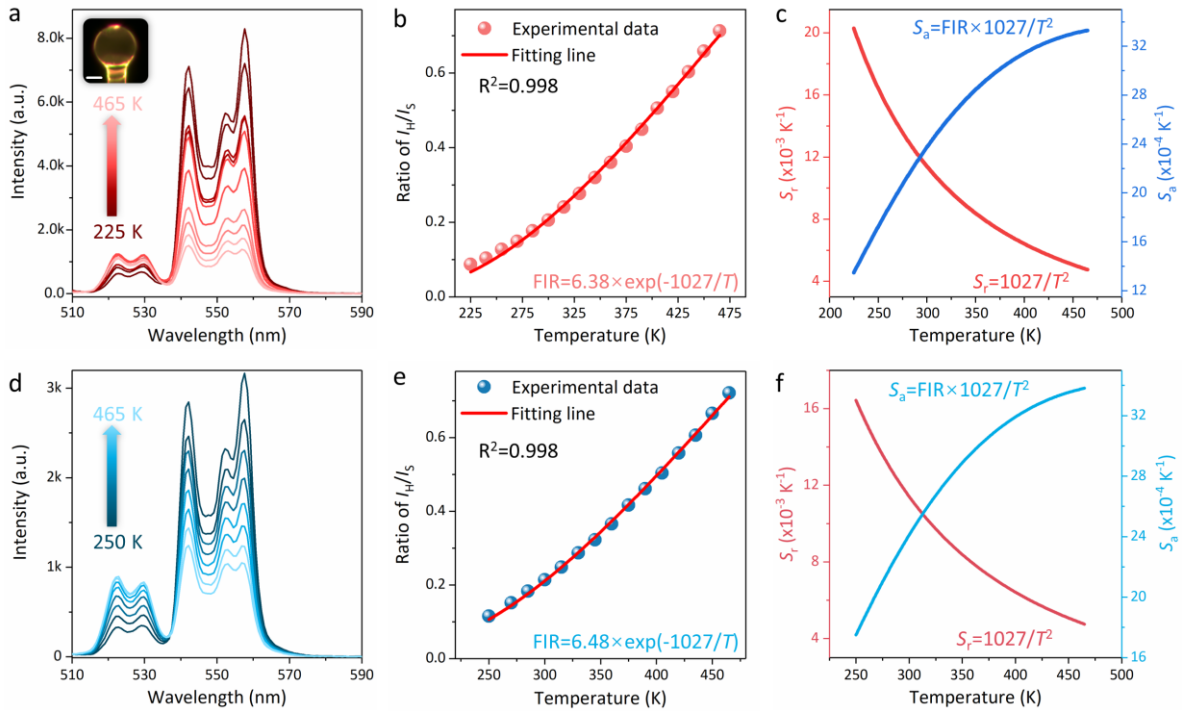

Fig. S12 Thermometric performance of the $NaYF_4$:20%Yb^{3+},2%Er^{3+}@$NaYF_4$ NC@FMS all-fiber temperature sensor in two continuous temperature change tests: (a) and (d) green fluorescence response to temperature; (b) and (e) experimental data and fitted curve of FIR ($^2H_{11/2}$/$^4S_{3/2}$) against the absolute temperature; (c) and (f) absolute and relative sensitivity. (a-c) are the results of the first continuous temperature change test, and (d-f) are the results of the second continuous temperature change test. The inset in (a) is the microscopic fluorescent photograph of the NC@FMS at room temperature. Scale bar: 15 μm.

To prove that the calibration curve of the designed NC@FMS all-fiber temperature sensor is also well reproducible, the starting temperature, some temperature points and excitation power were varied in the second continuous temperature change test. Under different test conditions, the green emissions change synchronously with the temperature, and the calibration curves show nearly no change, fully indicating the good reproducibility of the calibration curve, that is, the designed all-fiber temperature sensor has good reproducibility. The results in this Figure and Fig. 3 demonstrate the designed $NaYF_4$:20%Yb^{3+},2%Er^{3+}@$NaYF_4$ NC@FMS all-fiber temperature sensor with FMS size of ~50 μm has good stability, reproducibility, and accuracy, thus, it only performed one cycle of continuous temperature change test for the following studied NC@FMS all-fiber temperature sensors.

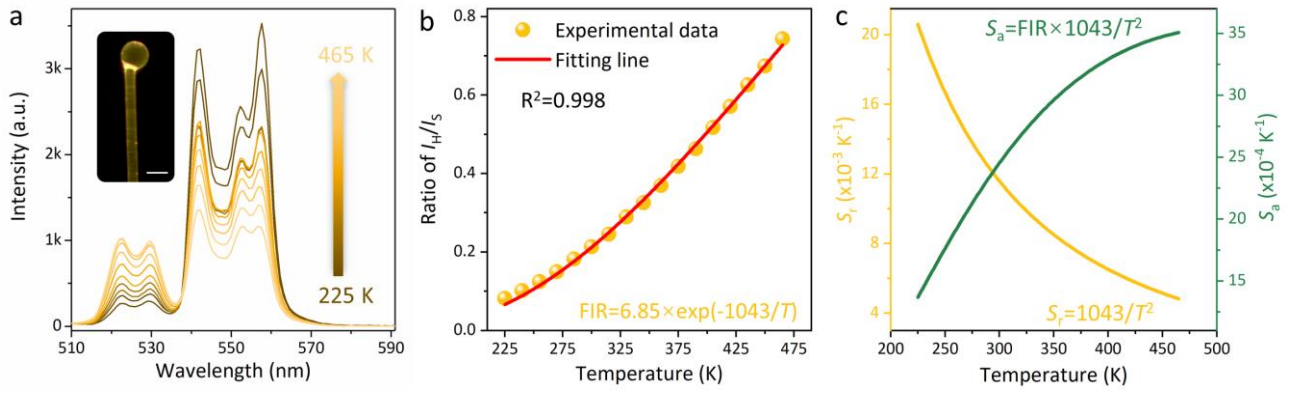

Fig. S13 (a) Green fluorescence response of the $NaYF_4$:20%Yb^{3+},2%Er^{3+} NC@FMS all-fiber sensor to temperature ranging from 225 to 465 K. The inset is the microscopic fluorescent photograph of the corresponding NC@FMS at room temperature. Scale bar: 40 μm. (b) Experimental data and fitted curve of FIR ($^2H_{11/2}$/$^4S_{3/2}$) against the absolute temperature. (c) Absolute and relative sensitivity of the $NaYF_4$:20%Yb^{3+},2%Er^{3+} NC@FMS all-fiber temperature sensor.

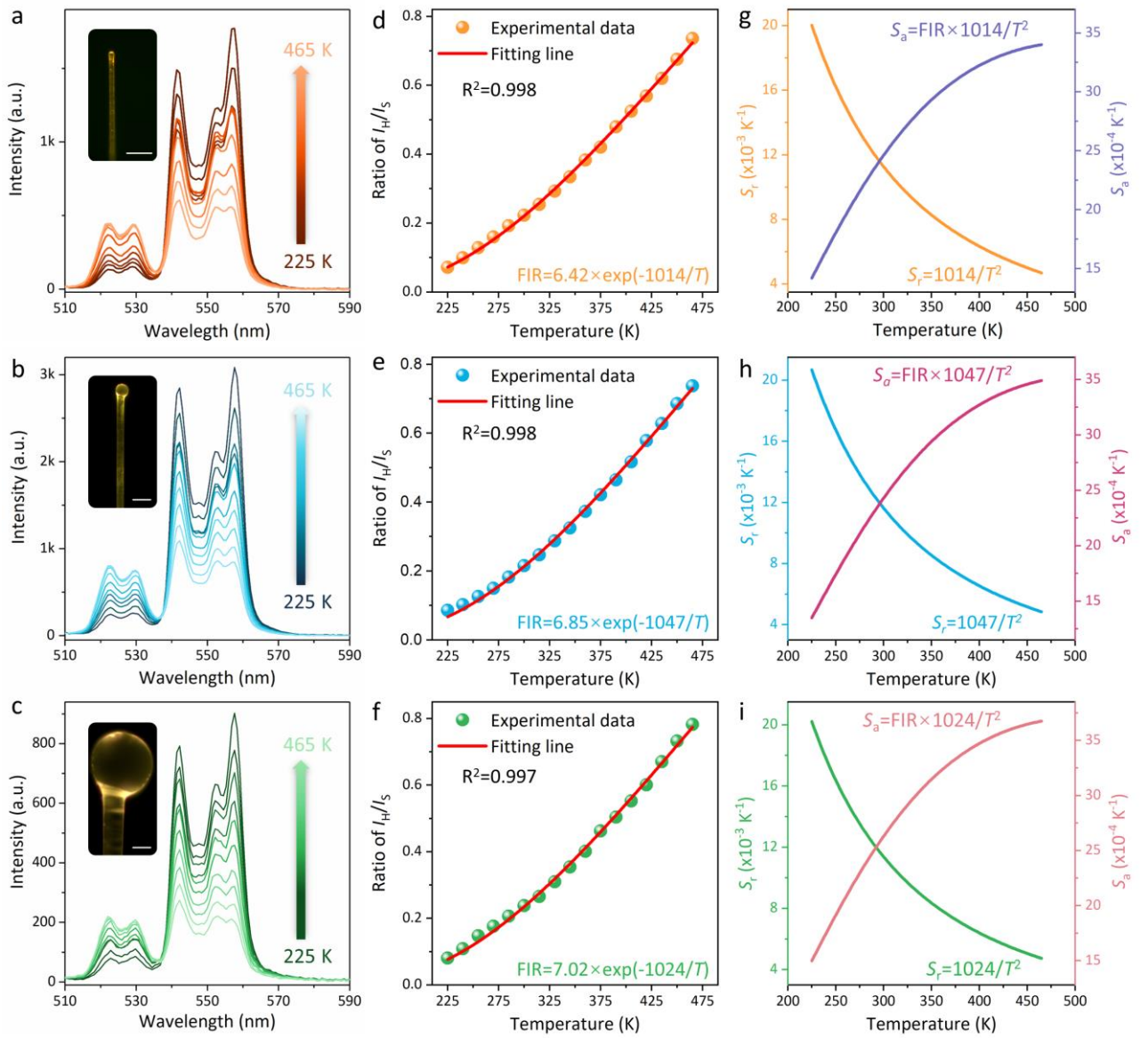

Fig. S14 (a-c) Green fluorescence response of $NaYF_4$:20%Yb^{3+},2%Er^{3+}@$NaYF_4$ NC@FMS all-fiber sensors with different microsphere sizes to temperature ranging from 225 to 465 K: (a) 8.5 μm; (b) 27.0 μm; (c) 136.2 μm. The insets are the microscopic fluorescent photographs of the corresponding NC@FMS at room temperature. Scale bars: 40 μm. (d-f) Experimental data and fitted curve of FIR ($^2H_{11/2}$/$^4S_{3/2}$) against the absolute temperature, corresponding to the all-fiber sensors in (a), (b) and (c), respectively. (g-i) Absolute and relative sensitivity of the $NaYF_4$:20%Yb^{3+},2%Er^{3+}@$NaYF_4$ NC@FMS all-fiber sensors in (a), (b) and (c).

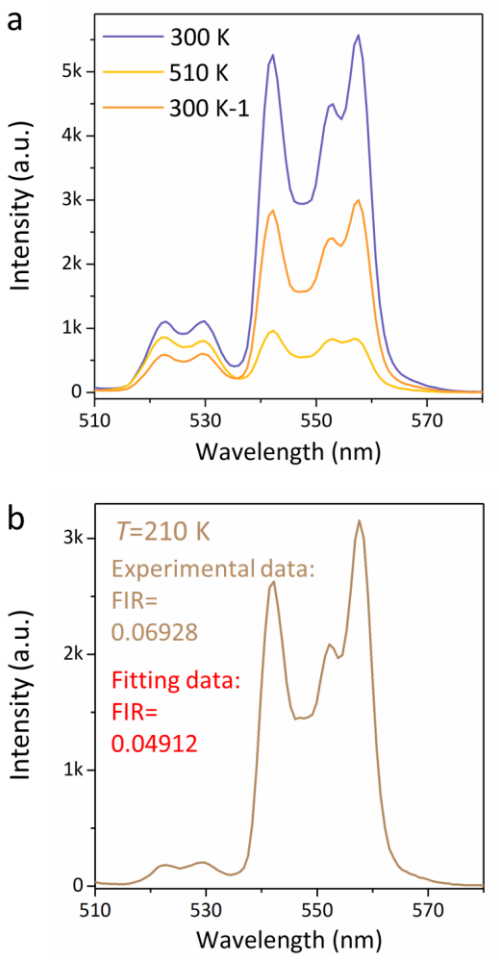

Fig. S15 (a) PL spectra of the $NaYF_4$:20%Yb^{3+},2%Er^{3+}@$NaYF_4$ NC@FMS all-fiber temperature sensor recorded at different temperatures. The "300 K-1" represents the spectrum after rising the temperature form 300 K to 510 K and then back to 300 K. (b) PL spectrum of the $NaYF_4$:20%Yb^{3+},2%Er^{3+}@$NaYF_4$ NC@FMS all-fiber sensor recorded at 210 K. In (b), the 0.06928 is the experimental FIR ($^2H_{11/2}$/$^4S_{3/2}$) data, while the 0.04912 is the fitting FIR data according to the fitting line in Fig. 3(b).

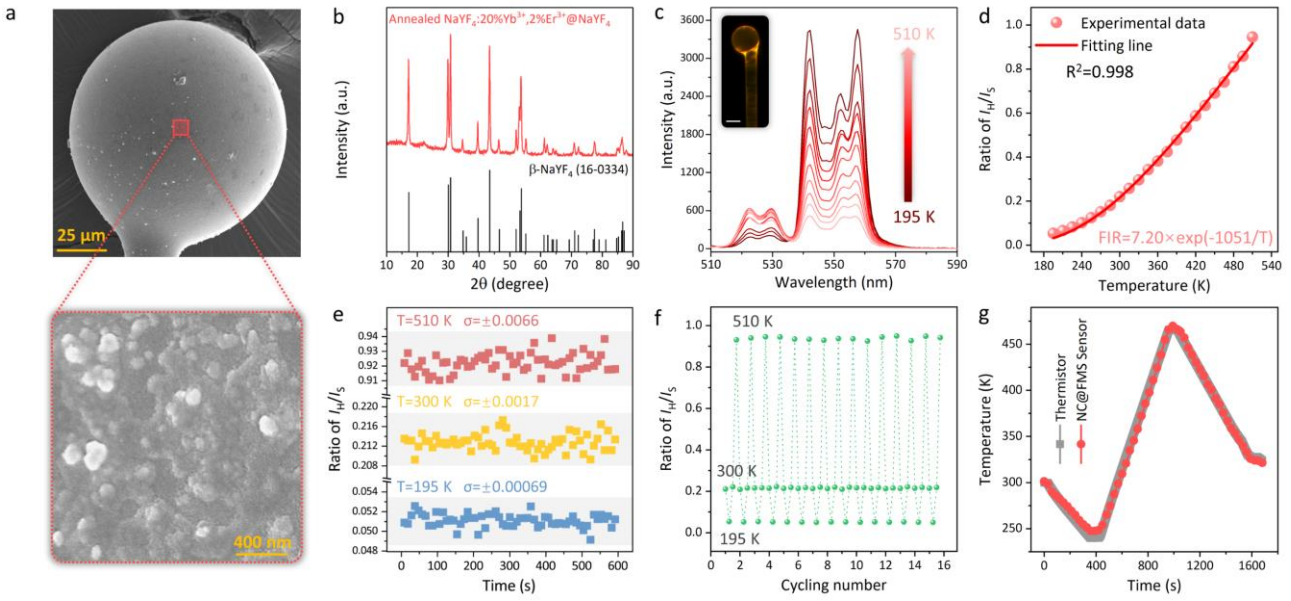

Fig. S16 Thermometric performance of the annealed $NaYF_4$:20%Yb^{3+},2%Er^{3+}@$NaYF_4$ NC@FMS all-fiber temperature sensor. (a) SEM images of the $NaYF_4$:20%Yb^{3+},2%Er^{3+}@$NaYF_4$ NC@FMS and its surface structures after annealing at 250 °C for 3 h. (b) XRD pattern of $NaYF_4$:20%Yb^{3+},2%Er^{3+}@$NaYF_4$ NCs annealed at 250 °C for 3 h. (c) Green fluorescence response of the annealed (250 °C for 3 h) NC@FMS all-fiber temperature sensor to temperature ranging from 195 to 510 K. The inset is the microscopic fluorescent photograph of the annealed NC@FMS at room temperature. Scale bar: 30 μm. (d) Experimental data and fitted curve of FIR ($^2H_{11/2}$/$^4S_{3/2}$) against the absolute temperature. (e) FIR ($^2H_{11/2}$/$^4S_{3/2}$) fluctuations of the annealed NC@FMS all-fiber temperature sensor over time at the constant temperatures of 195, 300, and 510 K. (f) Temperature cycling test of the annealed NC@FMS all-fiber temperature sensor between 195 and 510 K. (g) Comparison of the temperature response between a commercial thermistor and the annealed NC@FMS all-fiber temperature sensor.

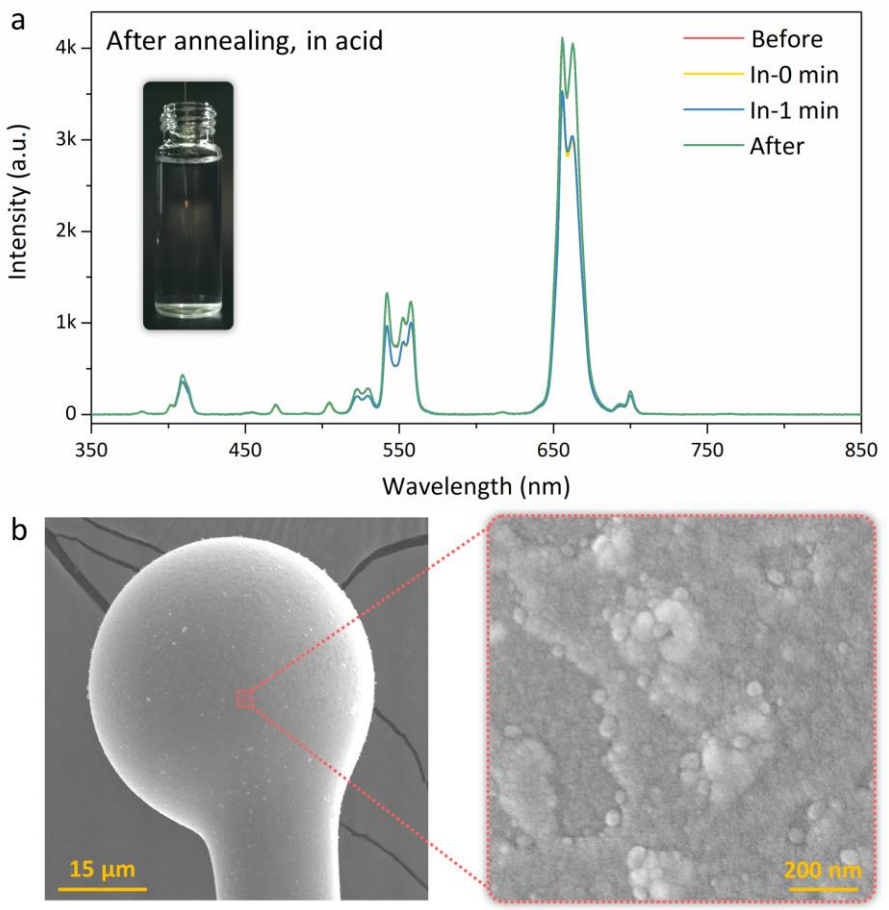

Fig. S17 (a) PL spectra of the annealed $NaYF_4$:20%Yb^{3+},2%Er^{3+}@$NaYF_4$ NC@FMS all-fiber temperature sensor before, during, and after immersing in an acidic environment for 1 min. The inset is the fluorescent photograph of the annealed NC@FMS when in the acidic environment. (b) SEM images of the annealed $NaYF_4$:20%Yb^{3+},2%Er^{3+}@$NaYF_4$ NC@FMS and its surface structures after immersing in the acidic environment for 20 min.

Table S2 Thermometric performance of the illustrative NC@FMS all-fiber temperature sensors in this work.

NCs	Size of FMS	ΔE (cm^{-1})	S_r (% K^{-1})	$S_{a\text{-max}}$ (K^{-1})
$NaYF_4$:20%Yb^{3+},2%Er^{3+}	53.2 μm	755.8	2.060 (225 K)	0.0035 (465 K)
$NaYF_4$:20%Yb^{3+},2%Er^{3+} @$NaYF_4$	8.5 μm	734.8	2.003 (225 K)	0.0034 (465 K)
$NaYF_4$:20%Yb^{3+},2%Er^{3+} @$NaYF_4$	27.0μm	758.7	2.068 (225 K)	0.0035 (465 K)
$NaYF_4$:20%Yb^{3+},2%Er^{3+} @$NaYF_4$	48.5 μm	744.2	2.029 (225 K)	0.0033 (465 K)
$NaYF_4$:20%Yb^{3+},2%Er^{3+} @$NaYF_4$	136.2 μm	742.0	2.022 (225 K)	0.0037 (465 K)
Annealed $NaYF_4$:20%Yb^{3+},2%Er^{3+} @$NaYF_4$	55.7 μm	761.6	2.076 (225 K)	0.0037 (465 K)

This Table summarizes the thermometric performance of the illustrative NC@FMS all-fiber temperature sensors in this work, including the calculated energy gap (ΔE), thermal sensitivity S_a and S_r with the optimal temperature. All these three values show small variations across the different sensors, indicating that the FMS and the fiber path only collect and transmit the optical signal and have no effect on the thermometric performance of the coated nanothermometers. It should be mentioned that the small differences among the different all-fiber sensors are due to slight temperature fluctuations during the temperature change test.

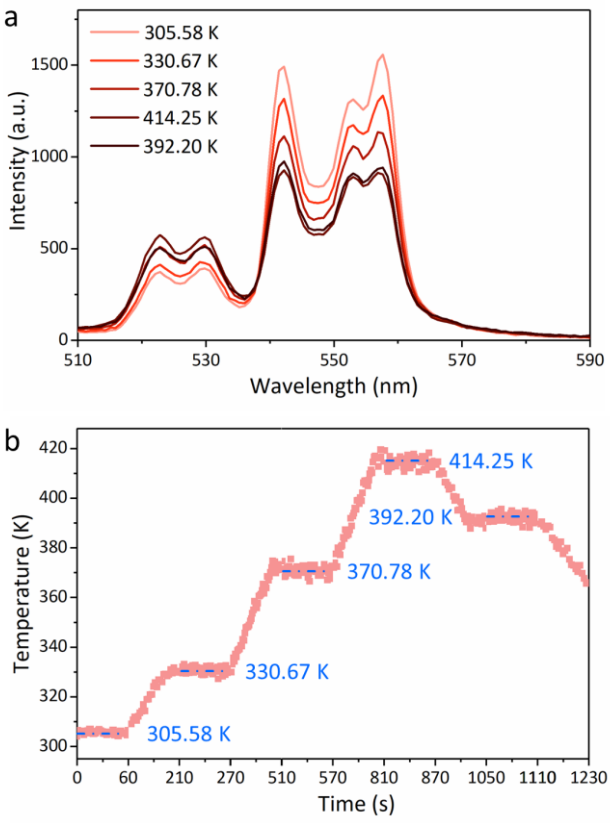

Fig. S18 (a) Fluorescence response of the $NaYF_4$:20%Yb^{3+},2%Er^{3+}@$NaYF_4$ NC@FMS all-fiber temperature sensor to temperature when placed in an enclosed space. (b) Temperature changes with time in the enclosed space obtained by using the NC@FMS all-fiber temperature sensor. The enclosed space is displayed in the inset in Fig. 4(c).

For this demonstration, as shown in Fig. 4(b), there is a hexagonal heating source in the enclosed space, and the NC@FMS was placed at a certain point above the heating source for temperature monitoring. Temperature program of the heating source was set to 308 K→333 K→383 K→433 K→403 K, and the temperature change rate was 15 K/min. There is a certain distance between the NC@FMS and the heating source, therefore, the detected temperature is lower than the heating source.

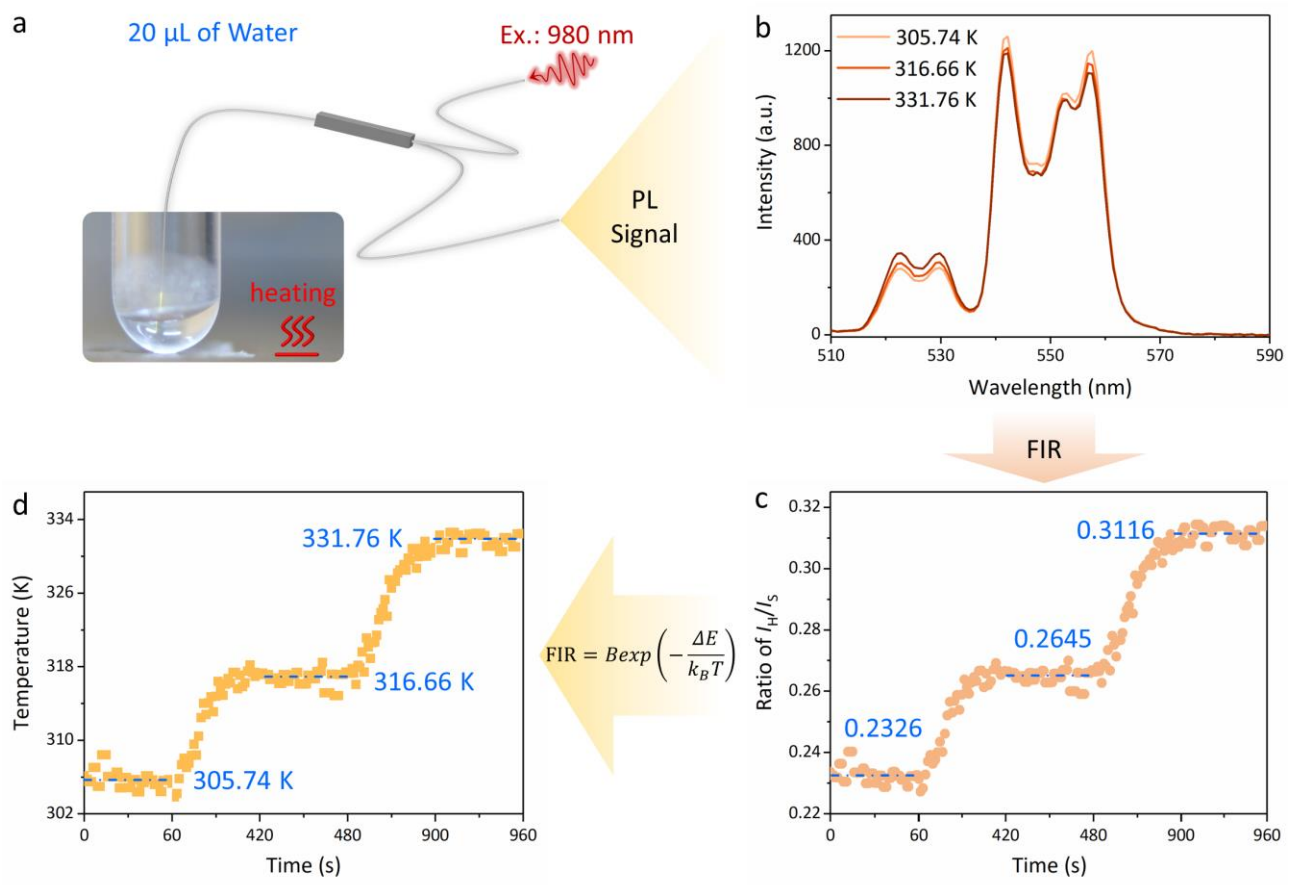

Fig. S19 (a) Schematic of the $NaYF_4$:20%Yb^{3+},2%Er^{3+}@$NaYF_4$ NC@FMS all-fiber temperature sensor monitoring the temperature of trace solutions. (b-d) Temperature changes with time in the 20 μL of heated water monitored by using the NC@FMS all-fiber temperature sensor. In this demonstration, a glass tube containing 20 μL of water was placed on a metal heater for heating, and the heating program was set to 308 K→318 K→333 K, with a heating rate of 5 K/min.

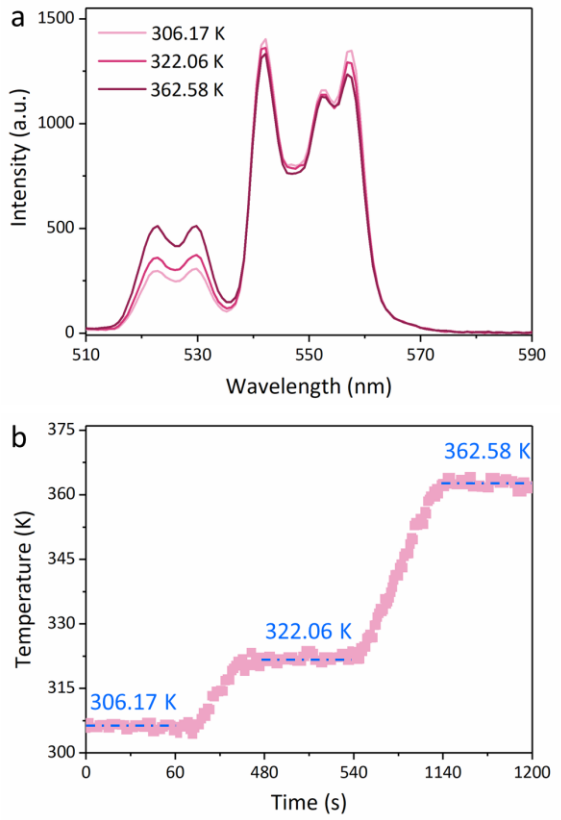

Fig. S20 (a) Fluorescence response of the $NaYF_4$:20%Yb^{3+},2%Er^{3+}@$NaYF_4$ NC@FMS all-fiber temperature sensor to temperature when used in 20 μL of heated ODE. (b) Temperature changes with time of the heated ODE obtained by using the NC@FMS all-fiber temperature sensor. In this demonstration, a glass tube containing 20 μL of ODE was placed on a metal heater for heating, and the heating program was set to 308 K→323 K→363 K, with a heating rate of 5 K/min.

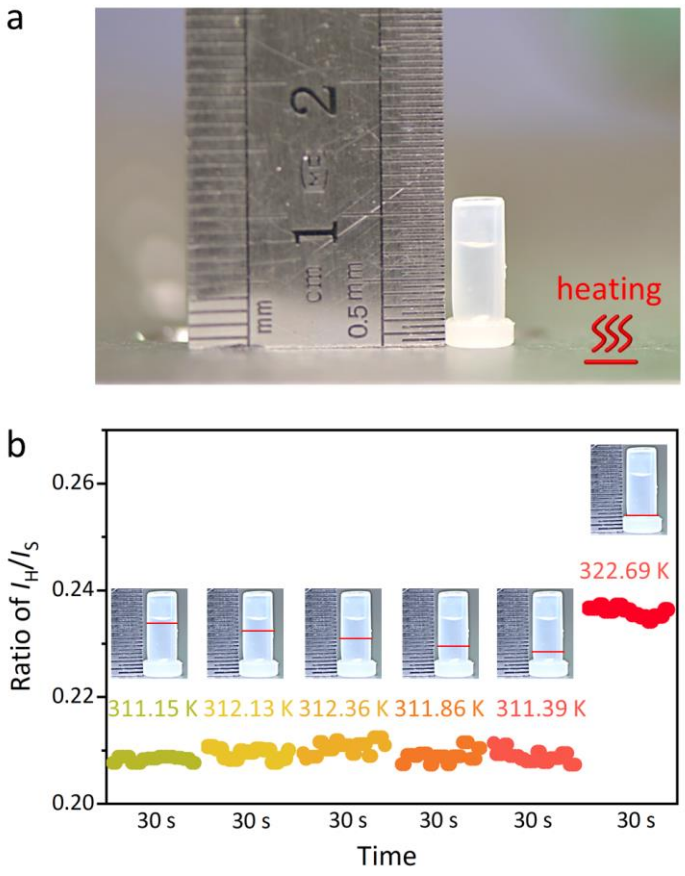

Fig. S21 (a) Photograph of the water used to demonstrate that the $NaYF_4$:20%Yb^{3+},2%Er^{3+}@$NaYF_4$ NC@FMS all-fiber temperature sensor can monitor temperature at different depths in a small amount of solution. (b) Temperature fluctuations at different water depths with 1 mm intervals monitored by using the NC@FMS all-fiber temperature sensor. The insets display the monitored water depth.

In this demonstration, a small plastic vessel with water was placed on the heating stage at a temperature of 343 K, as shown in (a). After heating for a certain time, the NC@FMS was placed in it to measure the temperature at different depths. Due to the poor thermal conductivity of the plastic vessel, the detected temperature is much lower than the heating temperature. Furthermore, it has a relatively high temperature close to the bottom owing to its thermalization at the bottom.

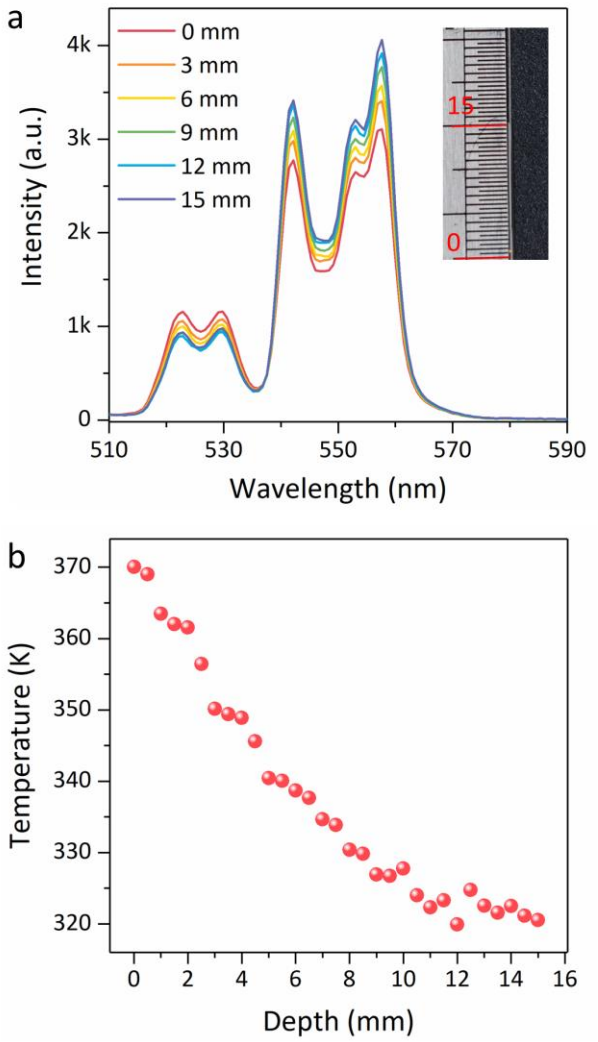

Fig. S22 (a) PL spectra of the $NaYF_4$:20%Yb^{3+},2%Er^{3+}@$NaYF_4$ NC@FMS all-fiber temperature sensor at different depths of a heated capillary tube. The inset shows the operating range of the NC@FMS all-fiber temperature sensor in the heated capillary tube. (b) Temperature changes with depth of the heated capillary tube obtained by using the NC@FMS all-fiber temperature sensor. The all-fiber sensor measured the temperature in every 500 μm.

For this demonstration, the capillary tube was fixed vertically on a heating stage at a temperature of 373 K. The NC@FMS was inserted into the capillary tube and measured temperature from near the heating stage with recording every 500 μm upward. As the NC@FMS moved away the heating source, the interior temperature of the capillary tube gradually decreases. This temperature gradient is consistent with the real situation, revealing the accuracy of the designed $NaYF_4$:20%Yb^{3+},2%Er^{3+}@$NaYF_4$ NC@FMS all-fiber temperature sensor.

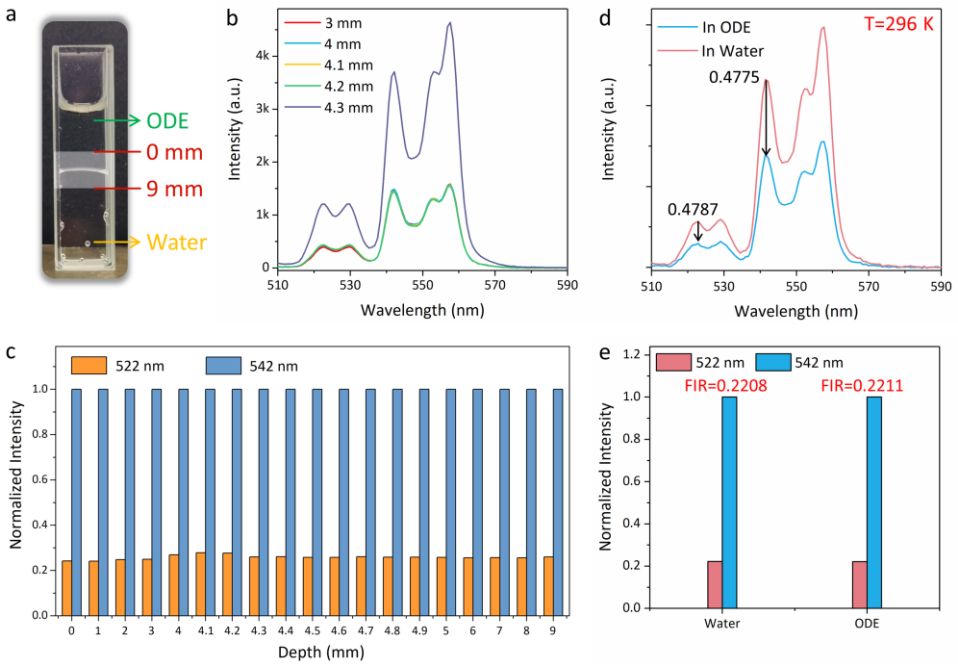

Fig. S23 (a) Photograph of the mixed solution of water and ODE, showing the operating range of the $NaYF_4$:20%Yb^{3+},2%Er^{3+}@$NaYF_4$ NC@FMS all-fiber temperature sensor in this mixed solution. (b) PL spectra of the $NaYF_4$:20%Yb^{3+},2%Er^{3+}@$NaYF_4$ NC@FMS all-fiber temperature sensor at different depths of the heated mixed solution. (c) Comparison of the emission intensity at 522 nm and 542 nm from the NC@FMS all-fiber temperature sensor at different depths of the above mixed solution. (d) PL spectra recorded for the same NC@FMS immersed in ODE and water at 296 K. The 0.4787 and 0.4775 are the relative intensity change from water to ODE for the emission peaks at 522 nm and 542 nm, respectively. (e) Comparison of the emission intensities at 522 nm and 542 nm and corresponding FIR values obtained for the same NC@FMS in water and ODE. For a clearer comparison, the emission intensities in (c) and (e) were normalized at 542 nm.

In this demonstration, a cuvette containing the mixture of water and ODE was placed on a heating stage at a temperature of 353 K. Heating for a while, the NC@FMS was inserted to measure the temperature near the interface. Due to the different refractive indices, the fluorescence intensities significantly increase from ODE to water, as shown in (b). It should be mentioned that the wavelengths at 522 nm and 542 nm are very close. Thus, the effect of the refractive index on the relative intensity change can be ignored. In (d), at the same temperature, these two wavelengths exhibit a close relative change from water to ODE, as a result, their FIR values in the two solutions are almost the same (see (e)). This result indicates that the calibrated NC@FMS all-fiber temperature sensor can be used for temperature sensing in different environments. The slight deviation of the FIR value between the water and the ODE should be a slight fluctuation of the test device, such as the spectrometer.

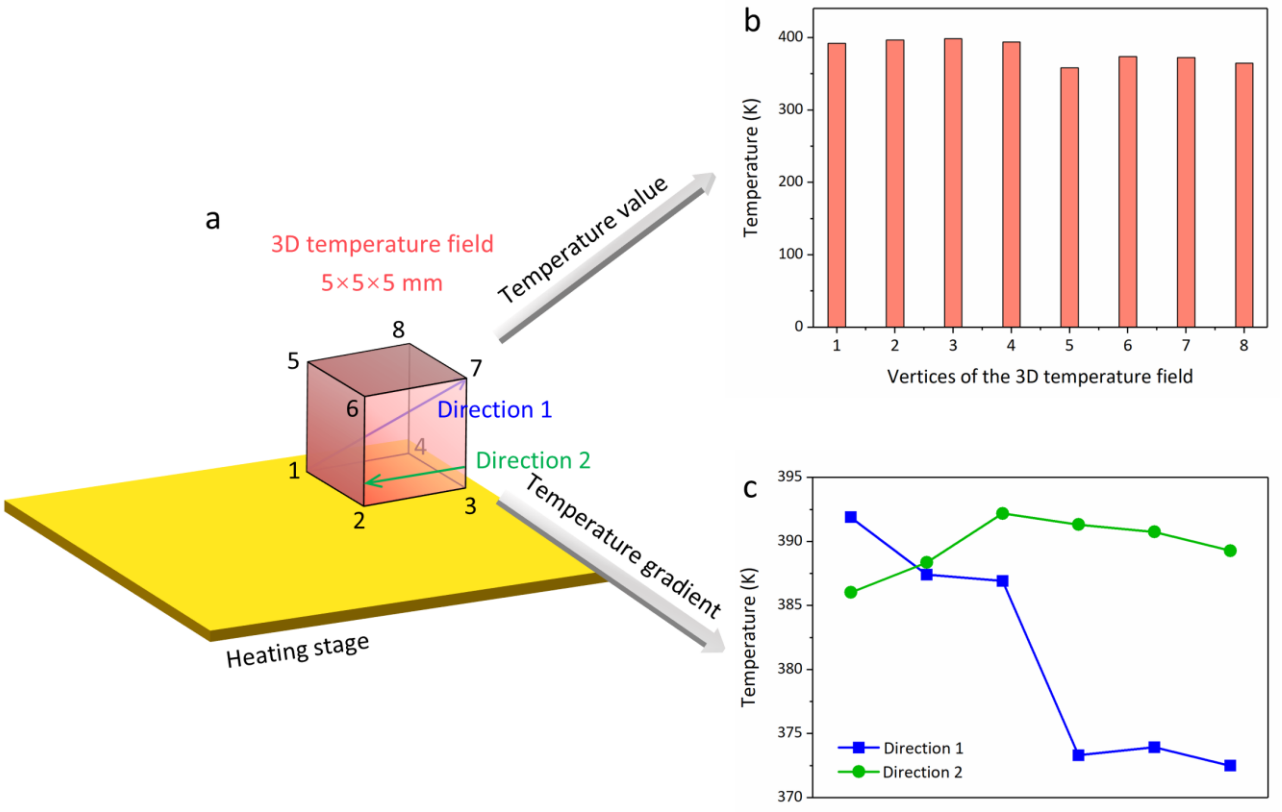

Fig. S24 (a) Schematic of the 3D temperature field in Fig. 5(a) illustrating the location of points to be measured in (b) and the arrows pointing the directions corresponding to temperature gradients in (c). (b) Temperature values of the eight vertices marked in (a). (c) Temperature gradient curves of the two directions marked in (a).

In this work, we drew a three-dimensional (3D) temperature map above a heating stage with a temperature of 423 K, as shown in (a). The heating source is in the center of the stage, and in order to achieve the temperature gradient, we chosen a 3D temperature field with a dimension of 5×5×5 mm at the upper left of the heating platform. By controlling the NC@FMS, we recorded one spectrum at 1 mm intervals in space, and then drew the 3D temperature mapping according to the spectra of the detected space points. The detected results show that the temperature decreases further away from the center of the stage, which is consistent with the real situation.

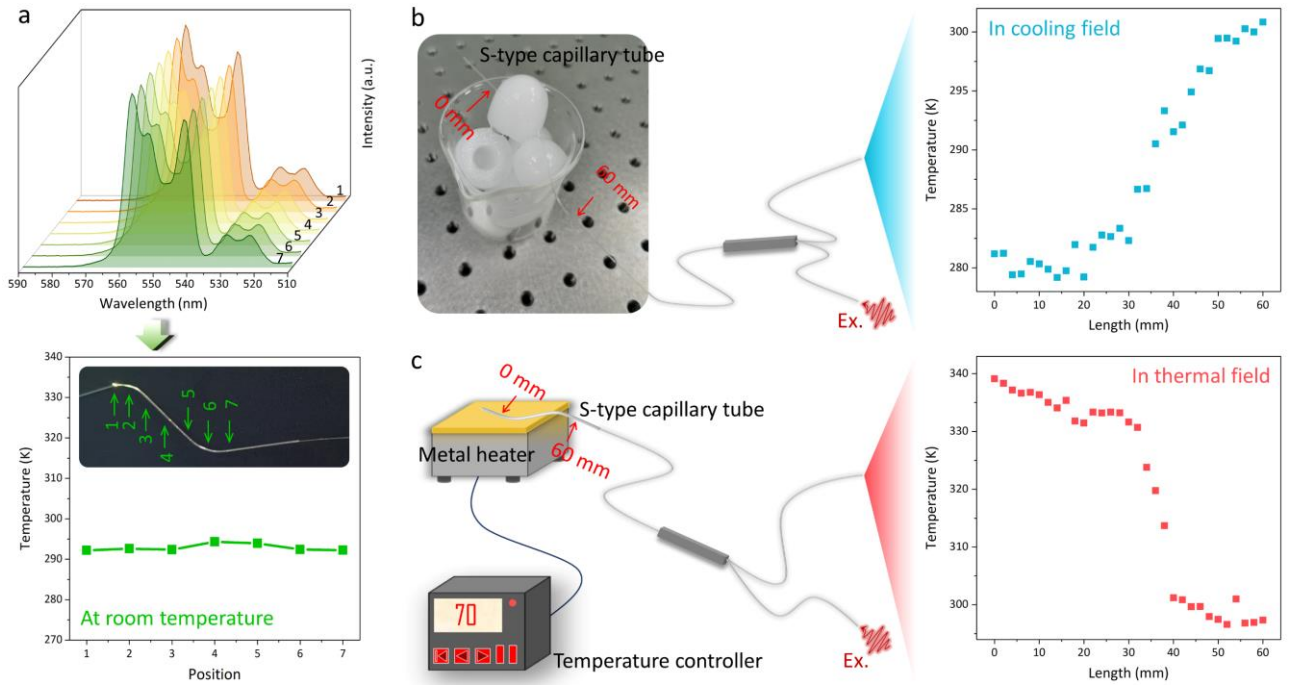

Fig. S25 (a) Interior temperature at different positions of a S-type capillary tube measured by using the $NaYF_4$:20%Yb^{3+},2%Er^{3+}@$NaYF_4$ NC@FMS all-fiber temperature sensor. (b) and (c) Interior temperature changes with length of the S-type capillary tube when in (b) a cooling field or (c) a thermal field monitored by using the NC@FMS all-fiber temperature sensor. The temperature sensor monitored the temperature at 2 mm intervals.

For the demonstration, in the cooling field, one end of the S-type capillary tube was placed on the ice, the other end was in the air (see (b)). The temperature rises gradually as the NC@FMS moves from 0 to 60 mm, which is consistent with the real case. While for the heating experiment, one end of the S-type capillary tube was placed on a metal heater, and the other end was exposed to air, as displayed in (c). The interior temperature drops gradually as the NC@FMS approaches to the edge of the metal heater, and drops significantly when the capillary tube is exposed to air. This temperature gradient is also as expected.

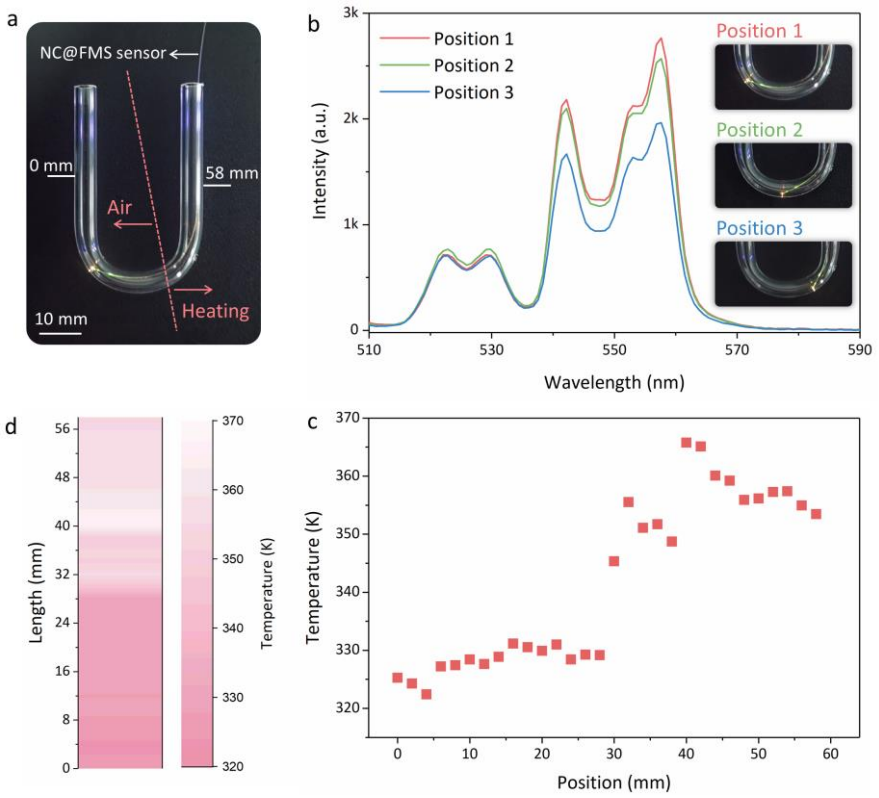

Fig. S26 (a) Photograph of the $NaYF_4$:20%Yb^{3+},2%Er^{3+}@$NaYF_4$ NC@FMS all-fiber temperature sensor working in a U-shaped tube, showing the operating range of the temperature sensor when one end of this U-shaped tube is placed on a metal heater with a temperature of 373 K, and the other end is exposed to air. (b) PL spectra of the NC@FMS all-fiber temperature sensor at different positions when the U-shaped tube is placed on the metal heater. The insets are the photographs of the NC@FMS all-fiber temperature sensor used for temperature measurement at corresponding positions. (c) Temperature changes with length of the U-shaped tube when placed on the metal heater measured by using the NC@FMS all-fiber temperature sensor. The temperature sensor measured the temperature at 2 mm intervals. (d) Temperature distribution mapping of the U-shaped tube when placed on the metal heater.

For this demonstration, a U-shaped tube with a diameter of 5 mm was used. Thus, after putting it on a metal heater, the internal vertical temperature is different, and the closer the metal heater is, the higher the temperature. When using the NC@FMS all-fiber temperature sensor to measure the internal temperature of the U-shaped tube, we measured the temperature at random positions of each point, not at the same horizontal position. In addition, our temperature sensor has a micron-scale spatial resolution. Hence, at the heated part, the measured temperature does not go from low to high regularly, but high and low. The overall trend of temperature change is consistent with the real case, which is that the closer to the heating center the higher the temperature.

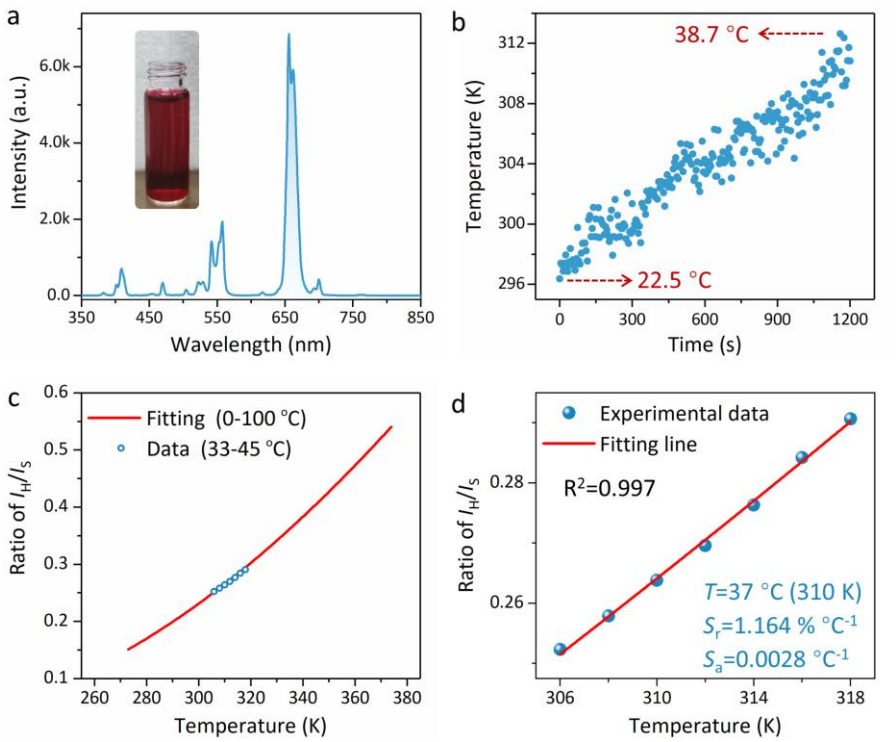

Fig. S27 (a) PL spectra and photograph of the $NaYF_4$:20%Yb^{3+},2%Er^{3+}@$NaYF_4$ NC@FMS all-fiber temperature sensor when inserted in the artificial blood at room temperature. (b) Temperature changes with time in artificial blood monitored by using the NC@FMS all-fiber temperature sensor. The artificial blood was placed on a metal heater, and the heating program was set to rise from 30 to 48 °C, holding for a certain time every 2 °C, and the heating rate was 3 °C/min. (c) Fitted curve of FIR ($^2H_{11/2}/^4S_{3/2}$) against the absolute temperature ranging from 0 to 100 °C and detected FIR ($^2H_{11/2}/^4S_{3/2}$) values with an interval of 2 °C. (d) Experimental data and fitted curve of FIR ($^2H_{11/2}/^4S_{3/2}$) against the absolute temperature ranging from 33 to 45 °C.